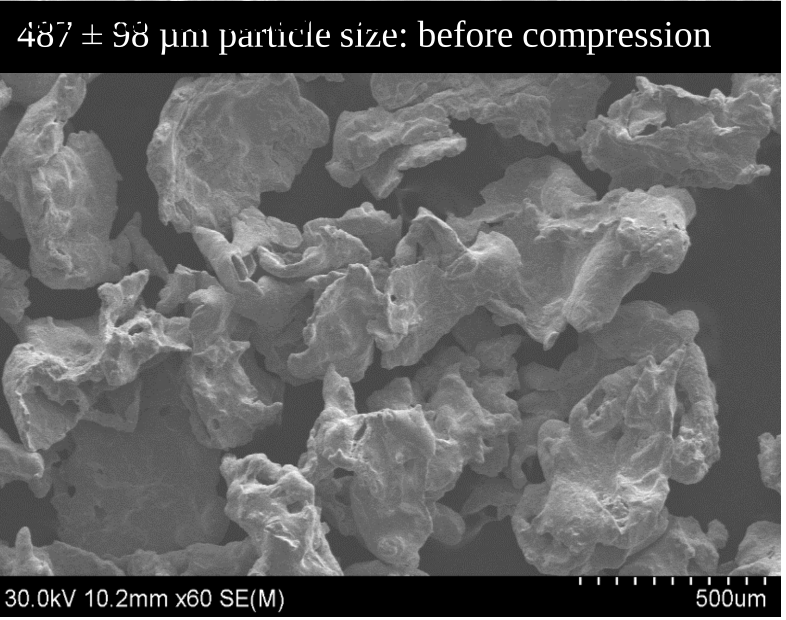

Figure 1 - In the figure above SEM images were taken of the SS316 powder at an average size of 487 μm before the material was compresses axially.

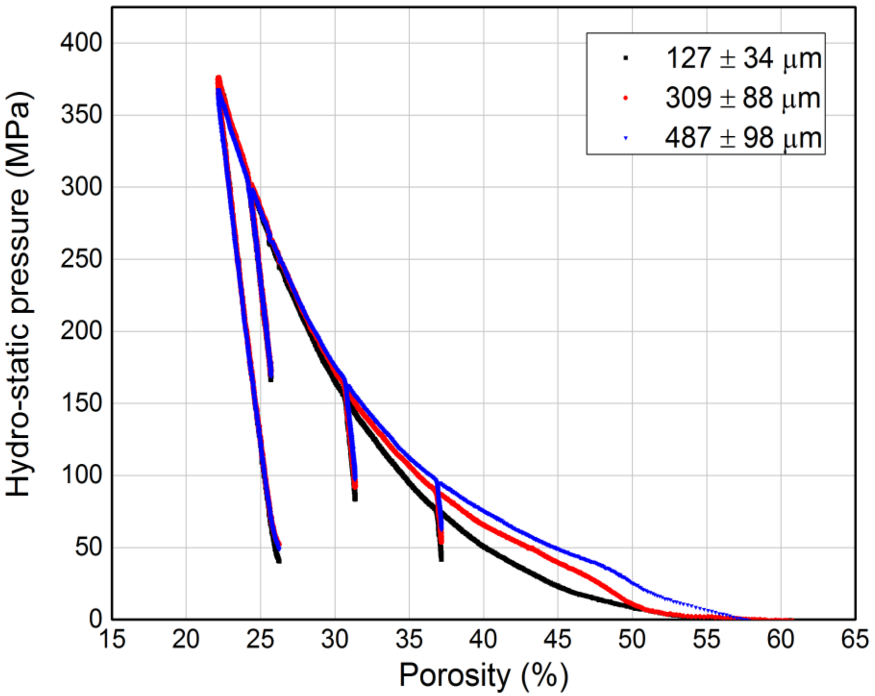

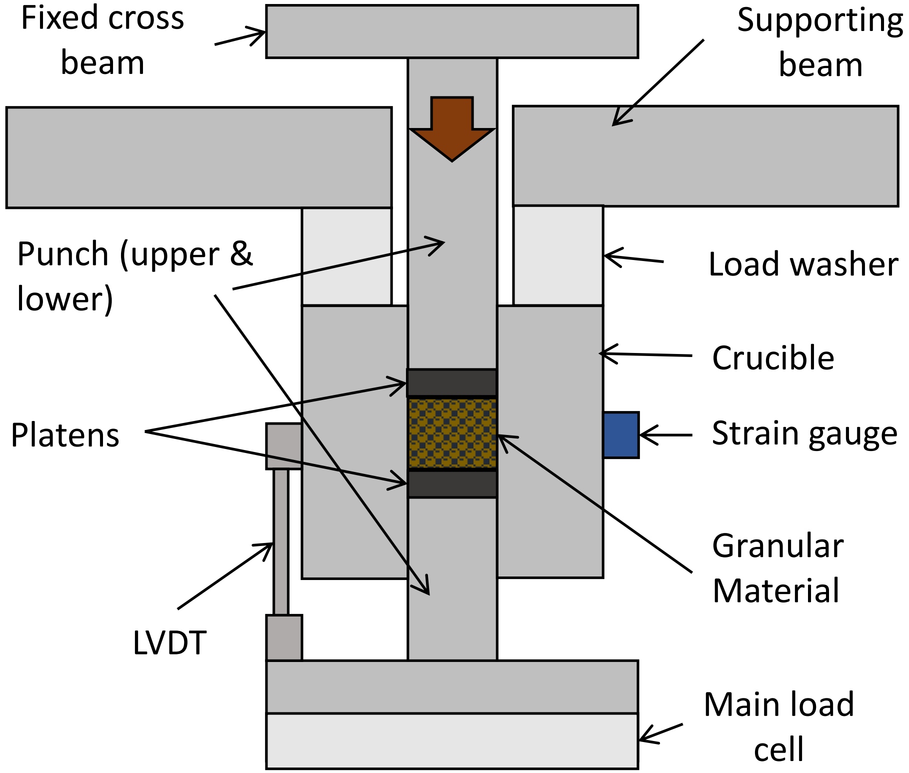

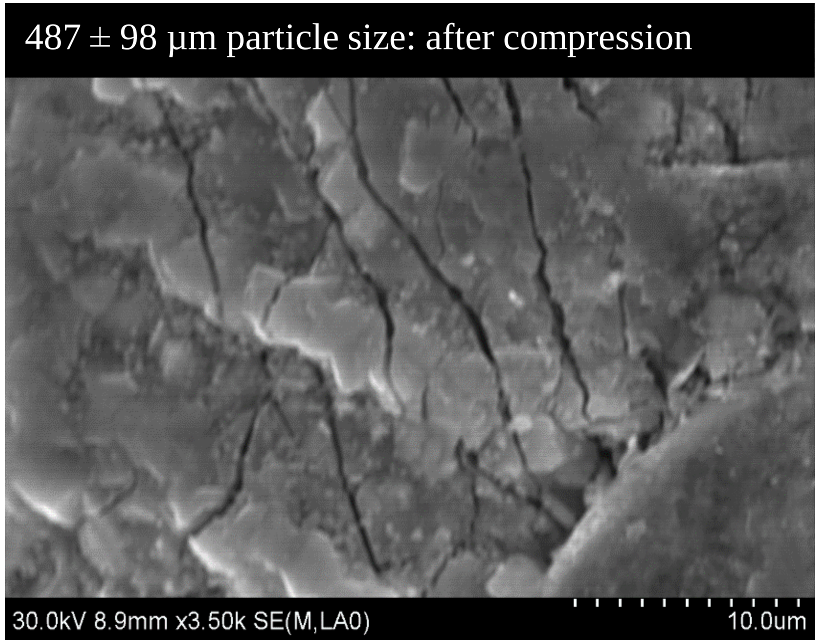

Figure 2 - Post-mortem SEM images were taken to visualize the mechanism responsible for material failure under compaction. Micro fractures were observed to be dominant.

***Highlights (for review)**

- Particle size dependents exists; for the porosity vs hydro-static pressure relation
- Bulk modulus: sensitive to the particle size and is dictated by different failure
- 127±34 µm particles exhibited higher stresses when compared to 487±98 µm particles

Confined Uniaxial Compression of Granular Stainless Steel 316

P. Nicewicz[a,1,*], T. Sano[b], J.D. Hogan[a]

[a] *Department of Mechanical Engineering, University of Alberta, Edmonton AB, T6G2R3*
[b] *Weapons and Materials Research Directorate, U.S. Army Research Laboratory, Aberdeen Proving Ground, MD 21005, USA*

Abstract

The quasi-static compaction response of granular stainless steel 316 was studied under triaxial loading conditions using a confined crucible experiment apparatus, specifically looking at effects of the particle size (127 ± 34 µm, 309 ± 88 µm, 487 ± 98 µm) on mechanical behavior. The material response was captured using load washer and strain gauges to relate: the porosity effects as a function of hydro-static pressure, particle size dependency on wall friction effects, and particle size-dependent failure mechanism. Our observations revealed that the path of crushing out porosity varied based on the particle size and the frictional effects. Scanning Electron Microscope (SEM) images were taken to observe the surface features of the compacted material and comment on failure mechanisms. Using these techniques it was observed that the smaller particles exhibited significant plastic deformation and flow, while the larger appeared to show micro cracking which lead to inelastic deformation and particle fracture. Altogether, these results are important because granular behavior is critical in powder flow applications such as additive manufacturing.

Keywords: Stainless steel, Granular, Triaxial compaction, Static, Failure of granular materials

1. Introduction

Granular materials are an agglomeration of discrete solid macroscopic particles that behave differently than continuous solids, liquids and gases. The understanding of granular behavior is critical in manufacturing [1], pharmaceutical [2], and geo-technical [3] applications. Researchers choose to pursue two main approaches when describing the granular behavior: discrete analysis and

*Corresponding author
[1]Email address: pnicewic@ualberta.ca

continuum mechanics. In the discrete approach, research is focused on individual particle behavior [4, 5, 6]. The discrete models are based on kinematics of the particles and allow for simulating mechanical characteristics [7]. More recently, discrete models exhibit deformability and allow for the simulation of the yielding behavior of materials [8]. Conversely, in continuum-scale studies researchers focus on using constitutive laws and conservation equations to model the ensemble of granular behavior [9, 10]. Specifically, researchers have derived a list of yield and friction models to express various characteristics such as variation in friction as a function of localized stress [7]. However, challenges exist with both approaches. Discrete modeling is computationally expensive and struggles with complex non-linear behavior [7, 11]. On the other hand, continuum models struggle with dry grains, for example, that do not support tension. This means the behavior changes from plastic media to a gas-like disconnected state which is difficult to represent in a unified model [9]. Researchers have been interested in the micro-scale of solid-like behavior of grains [12] while capturing the macro-scale fluid-like characteristics [13] due to the large application possibilities. Challenges exist when working with granular materials and so, to address this issue, the current study of granular media has been undertaken by looking at granular failure in cold press compaction.

The compaction of cold-pressed powder is of particular interest to pharmaceutical researchers [14], when looking at particle distribution, Jansen coefficient for particle friction, and porosity as a function of applied stress [2, 15]. For example, Michrafy et al. [15] studied the frictional effects of pill compaction lubricant effects on the Columb wall friction coefficient. They showed that wall friction and particle friction primarily account for non-uniform stress distribution and produce a density gradient of the material in the compact; the lack of consistent density results in skewed mechanical properties [16]. Similar work was conducted by Kadiri et al. [14]. They looked at predicting the axial density distribution of microcrystalline material while determining the material properties during quasi-static triaxial compression. The axial density of cellulose decreases from the top to the bottom of compaction and Kadiri et al. [14], concluded that the particle size and shape significantly influence the density distribution throughout pharmaceutical tablet compaction.

Similar work on cold compaction of granular materials has been conducted in additive manufacturing (AM), where it is important to understand the relationship between the powder characteristics and the mechanics of the consolidated part [17, 18]. For example, mechanical properties, surface finish, and integrity of the final structure are highly influenced by the characteristics of the powder material that is used in the manufacturing process. Further, flowability of the powder highly influences the finish, grade, and strength of the final product. The correlation between factors such as the shape distribution, size distribution, density, and packing density are a complex and an ongoing research topic [19]. In one example, Spierings et al. [20] determined that larger stainless steel (SS316) particles in the raw powder consequently resulted in bigger pores in the final steel part. Thicker layers created inhomogeneous regions in the structure that promoted fracture [20] and increased void density creates nucleation sites for brittle failure, and promotes crack propagation. Comparable research was done by Bai et al. [21] when analyzing the binder jetting AM technique with copper particles. Similar to laser sintering, binder jetting combines the metal powder with a binder and creates a semi consolidated green structure surrounded by the remaining powder, which is then sintered. By using a bimodal powder distribution, Bai et al. [21] was able to improve the powder density by 8.2 % and flowability by 10.5 %. Powder flow properties (flowability) has been shown to play an important role in the cohesive strength, friction, compressibility, and transportation of the powder [19, 22]. The tailoring of particle sizes is required to improve the final density of the structure.

In this study, we are primarily concerned with the behavior of granular stainless steel particles. Due to its high hardness and elasticity, stainless steel 316 (SS316) powder has been used in various industry applications. These applications include making artificial joints in medical research [23], creating tooth implants in the dentistry industry [24], and as a AM material in creating complex geometries in the manufacturing industry [17]. To optimize the usage of SS316 powder in the various industries, the shortcomings of powder flowability and particle variability relating to strength must be addressed and understood [17]. Further research is required to obtain a better understanding between particle characteristics, strength, and product performance. Previous research shows a gap in understanding the behavior of particles in granular material. Addressing this gap would improve the repeatability of manufacturing and the final performance of the products by limiting the large variation we see in granular SS316. The behavior of granular SS316 is studied in this paper with an emphasis on the effect of particle sizes on flow behavior and particle variability in strength. A uniaxial confined experimental technique is used to evaluate the triaxial flow stress SS316 exhibits for increasing particle sizes. This allows for progress in evaluating accurate failure mechanisms in the material and linking the overall effects of particle size on material behavior. In this paper we investigate the effects of hydrostatic pressure and porosity of the SS316 powder. Further, we look at the relationship between the axial and radial stress to comment on the Janssen coefficient as a function of changing particle size. Lastly, we are interested in the loading and unloading behavior of the SS316 powder observing the changing stiffness degradation and material behavior. By addressing these areas, advancements will be obtained to better understand the effects of particle size on strength and part quality where stainless steel particles are used.

1.1. Experimental Techniques

1.2. Material

1.2.1. Composition and Geometry

SS316 powder was used in the experiment and the elemental composition was provided by the manufacturer and is summarized in (Table 1). The elemental breakdown is typical for SS316. The powder was sourced from Alfa Aesar by Thermo Fisher Scientific of Tewksbury, Massachusetts. The average particle sizes used for the triaxial compaction were three different size ranges: 1. 127 ± 34 µm, 2. 309 ± 88 µm, and 3. 487 ± 98 µm.

The SS316 powders used, range from 127 µm to 487 µm in size and exhibit a rough irregular shape. This is most likely due to the manufacturing process of using water atomization to create the powder [25]. For visual aid, the powder geometry is illustrated in Figure 1 for sieved particle sizes: 309 ± 88 µm and 487 ± 98 µm. The images were taken with a Hitachi S-4800 Field Emission Scanning Electron Microscope (SEM).

1.2.2. Particle Distribution

Three different sizes were sieved, microscopically analyzed, and tested to observe the effects of mean particle diameter, Ø (µm), on hydro-static pressure as a function of porosity. The mean and standard deviation was documented for each particle size for the range of: 127 ± 34 µm, 309 ± 88 µm, and 487 ± 98 µm, summarized in Table 2. The particle sizes were chosen based on the restrictions of the crucible design and access to materials with a higher Rockwell hardness. Every specimen tested was separately analyzed and sampled following principal sampling techniques for granular material outlined by Maynard [26].

The particle size distribution and shape was analyzed using the automated Malvern Morphologi G3 microscope (G3). The De Broukere mean diameter (volume moment mean diameter) was considered when anlyzing the particle sizes. This parameter is most relevant when determining the distribution of the bulk sample used in experiment and has been used by many in literature [27, 28]. The definition of this relation is on the basis of introducing another linear term in diameter, analogous to moments of inertia i.e. accounts for the center of gravity of the particle distribution. The next point to underline is that the advantage of this method does not require the particle count. This was done by taking the square difference of the upper and lower bin to determine D_i which determined the mean particle distribution in the sample. The numerator is taken to the power of four (the power of three to account for the equivalent volume and the additional power to account for the center of gravity) and the denominator is taken to the power of three (where it accounts for the mass of the particles). Seen below is the summarized equation:

$$D[4,3] = \frac{\sum_1^n D_i^4}{\sum_1^n D_i^3} \tag{1}$$

To evaluate the variability of the powder, the span, Δ, was calculated for each sample, as was similarly used by Engeli et al. [29]. The span was determined through the following and this takes into account the tenth (D_{10}), fiftieth (D_{50}), and ninetieth percentile (D_{90}):

$$\Delta = \frac{D_{90} - D_{10}}{D_{50}} \tag{2}$$

The particle size based on (1) and the span of the distribution based on (2) are summarized in Table 2. With an increase in mean particle diameter, the standard deviation increases while the span decreases, highlighted in Table 2. These particle statistics are considered later when mechanical behavior is investigated.

Particle shapes were also considered. Shown in Table 2, the average circularity, C, of the particles decreases as the average particle size increase. Circularity refers to how close the particles resemble a perfect sphere. Less circular particles have a larger deviation in the particle size. The circularity of the material is directly related to the manufacturing process such that the method of atomization dictates the final shape of the particle [25]. Here we computed particle circularity(C) defined as:

$$C = 2\sqrt{\frac{\pi A}{P}} \tag{3}$$

where A, (m^2), and P, (m), are the area and perimeter of the particle, respectively. As the particles increase in mean diameter the circularity decreases. The shape results are important because as noted by Schade et al. [19] the decrease in circularity causes the particles to align in other orientations and ineffectively fill in the voids. Schade et al. [19] determined that the difference in circularity is related to the atomization process of the granular material i.e. gas atomization produces spherical shaped particles and water atomization produces rough, irregular particles.

1.3. Quasi-static compression

1.3.1. Configuration

Illustrated in Figure 2 is a schematic of the experimental apparatus used to conduct confined uniaxial compression experiments on the granular material to obtain a triaxial response. The top punch, bottom punch, and platens are fabricated from D2 tool steel and were heat treated using quenching and double tempering to reach a hardness of 62 HRC. The punches are used to press together the platens that contact the granular material. The top and bottom punches are designed around the accessibility of the MTS 810 machine used in this study, and are 130 mm in length. The crucible was made out of 4340 steel and heat treated by quench and tempering followed by gas nitriding. The maximum hardness achieved was 52 HRC with an inner and outer diameter of 6.3 mm and 22.2 mm, respectively. The inner diameter was machined with a tight tolerance so that the sacrificial platens were able to seal in the granular material and to protect the punches from the granular media. The supporting beam, designed out of aluminum, was placed to differentiate between the normal forces on the top and bottom of the sample. The support beam is held up with aluminum blocks that attach to the MTS. Aluminum supports were designed for attaching the linear variable differential transformer (LVDT) so that relative displacement could be recorded to minimize the deflection during compression. The operating parameters for the LVDT were $\pm$ 7.5 mm and 0.2 % linearity error. The MTS machine outputs the applied load at a rate of 0.33 kN s^{-1} with a resolution of 305 µV per analogue-to-digital converter count, placing the specimen in a quasi-static stress state. Between the top punch and the crucible is a load washer from Omega Engineering Inc. The operating parameters for the load washer was 10 kN with an accuracy of $\pm$ 0.5 %.

For specimen preparation, one end of the crucible was closed using the platen and punch. In order to limit the wall frictional effects occurring during confined compaction it is critical to maintain an aspect ratio of height to width of < 1 when determining the sample size [30]. Granular material was poured in and an aspect ratio of 0.76 ± 0.05 was achieved. The volume of material needed to satisfy this constraint is 150.8 ± 3.3 mm^3. Sample volume was not the same for all samples and the uncertainty reflects the variation.

The supporting beam illustrated in Figure 2 creates a free floating state such that the compaction of the material is not affected by the weight of the crucible. The top punch was lowered, rested against the platen on the top of the specimen with the assumption that the specimen has not been compacted. A linear variable differential transformer (LVDT) was secured to the beam, so that the compaction depth could be measured relative to the displacement. The load washer was used to measure the combined frictional effects during the uniaxial compression. Next, we outline the theory used to interpret the measurements.

1.3.2. Theory

To better understand the response of the granular material during quasi-static triaxial compression, we investigate the relationship between the hydrostatic pressure and porosity by tracking the volumetric strain and relative density in the confined crucible. First, we track the time-evolving reduction in porosity of our test samples through measurements of initial mass m (kg), initial packing porosity ϕ_i (%), and the cross-head displacement δ (mm) of a plunger that is used to compress our granular samples. The mass of the initial granular sample is measured by a digital scale with the precision of 0.01 g. The size of each samples was controlled by volume ($\sim$150.8 mm^3). Throughout the compression experiment, the change in volume, ΔV (m^3), is related to axial displacement:

$$\Delta V = A_0 \delta \tag{4}$$

where A_0 is the cross-section area of the void (m^2) and δ is the relative axial displacement during compression (m). From there, we can calculate the specimen density ρ as it evolves during compaction:

$$\rho = \frac{m}{V_0 - \Delta V} \tag{5}$$

where m is the mass of the specimen (kg), and V_0 is the initial specimen volume (m^3). The evolving porosity is calculated by normalizing the specimen density with the solid bulk density:

$$\phi = 1 - \frac{\rho}{\rho_s} \tag{6}$$

where ϕ is the porosity fraction (unit less) and ρ_s is the bulk solid density (kg m^{-3}). For stainless steel the bulk density is taken as 8000 kg m^{-3}, which provided by the manufacturer.

Next, the hydrostatic pressure is calculated by measuring the axial stress, σ_{zz} (MPa), from the MTS machine and the radial stress, $\sigma_{\theta\theta}$ (MPa), measured from mounted strain gauges on the crucible, see schematic in Figure 2. The equation for hydro-static stress, σ_{hyd} (MPa), in cylindrical coordinates is defined as [31]:

$$\sigma_{hyd} = \frac{1}{3}\left(2\sigma_{\theta\theta} + \sigma_{zz}\right) \tag{7}$$

We calculate σ_{zz} by dividing the axial force experienced by the sample, F_{zz} (N), and the cross-sectional area of the void A_0 (m^2), assuming that the area does not significantly deform during compression:

$$\sigma_{zz} = \frac{F_{zz}}{A_0} \tag{8}$$

F_{zz} was computed by subtracting the axial force outputted by the MTS machine, F_{MTS}, and the friction forces, F_f (N), induced by the platens and granular powder contacting the crucible walls:

$$F_{zz} = F_{MTS} - F_f \tag{9}$$

To determine the radial stress, we assumed the crucible was a thick walled cylinder (TWC). The TWC equation assumes that the crucible geometry is symmetric on θ (°) and the stress is only a function of r (m). The problem is statically determinate and so only the equilibrium equations must be satisfied. The derivation of the equilibrium equations along with the solution have been computed extensively in literature and therefore will not be explicitly shown (see reference [31] and [32] for full derivation). Equation (7) can be rewritten to include the axial stress and radial stress to obtain an expression for hydro-static pressure as a function of measurable parameters:

$$\sigma_{hyd} = \frac{1}{3}\left(\frac{F_{zz}}{A_o} + E_{cr}\varepsilon_{\theta\theta}\frac{b^2 - a^2}{a^2\left(1 - \nu_{cr}^2\right)}\right) \tag{10}$$

where E_{cr} (MPa) is the stiffness of the crucible, ν_{cr} is Poisson's ratio of the crucible, a is the inner radius (m), b is the outer radius (m), and $\varepsilon_{\theta\theta}$ is the radial strain as a function of thickness [31]. There are, however, limitations of using the TWC approach which has been identified by, for example, Kim et al. [33]. According to their research, shortcomings exists when measuring hoop strain. This is dependent on the inner diameter, cylinder thickness, and location of strain gauge along the axial direction. In our apparatus, the inner diameter is much smaller than the diameter tested by Kim et al. [33], further, when extrapolating from the two sizes that were compared, our void size is proportional to the maximum strain we measured. In addition, the strain gauge size and placement encompassed in our experiment the entire testing section and so we think that some of the uncertainty in the measurements is mitigated.

Next, we look at the bulk behavior of the material. This characteristic describes the compressibility of the material and relates the change in pressure of the material with respect to volume. This is given by:

$$B_{ep} = \frac{\sigma_{hyd}}{\frac{\Delta V}{V_o}} \tag{11}$$

where B_{ep} represents the bulk modulus taking into account elastic and plastic behavior (MPa), and all the other variables have been previously defined. This parameter evolves during loading and is an indicator of deformation in the granular sample. Similar calculations were done by Gustafsson et al. [34] when conducting confined compression experiments with iron ore.

We also consider the axial-to-radial effects by calculating the Janssen coefficient of SS316 powder. This parameter relates the radial and axial stresses during compaction which allows for simplification when conducting computer modeling of the compaction [35]. The Janssen constant, K, is given by:

$$K = \frac{\sigma_{\theta\theta}}{\sigma_{zz}} \tag{12}$$

Lastly, we look at frictional effects by monitoring the transmitted stress ratio, T (unitless). To do this, we calculate the ratio of transmitted stress, σ_t (MPa), over applied stress, σ_a (MPa). The applied stress is the stress that the compression machine outputs and the transmitted stress is the stress that is interpreted from the load washer. The difference in applied and transmitted stresses provides insight on how much energy is lost to friction in the crucible apparatus. This ratio is given by:

$$T = \frac{\sigma_t}{\sigma_a} \tag{13}$$

To account for the uncertainty in the experiment, we conducted a systematic propagation of error, taking into account the uncertainty of the sensors and measured geometries. This will help in understand the accuracy of our results. Based on the guide outlined by Berendsen [36], Table 4 summarizes the relative uncertainty of critical material parameters that were calculated. The rules for calculating uncertainty have been derived and computed extensively in literature and will not be explicitly shown. Refer to [36] for full derivations.

2. Experimental Outcome

2.1. Porosity

As an outcome of the confined uniaxial compaction, we first investigate compressibility, loading path, average particle diameter and geometry of the material. As a limitation to this work, additional tests should be conducted and a wider range of particle sizes should be included to account for any outlying behavior. Shown in Figure 3 is the relationship between the hydro-static pressure and porosity for three different particle size ranges; 127 ± 34 µm, 309 ± 88 µm, 487 ± 98 µm. The initial porosity for each test was 60 % for size 127 ± 34 µm, 66 % for size 309 ± 88 µm, and 67 % for size 487 ± 98 µm. From the initial porosity to a porosity of 30 %, the curve of each particle size behaves differently for each sample. For porosities above 30 %, smaller particles have lower hydro-static pressure. For porosities less than 30 %, the relationship between porosity and hydro-static pressure collapses onto a single curve for each particle size range studied. Prevoius work by Heckel [37] noted simlar results when studying metalic powders such as iron, nickel, tungsten, and copper. Linear-like trends were observed for compressive stresses applied >135 MPa . In addition, no difference in load-unload behaviors are observed across all particle sizes for a given porosity. As the hydro-static pressure is reduced, the effect of unloading results in incremental increases in porosity (the linear curves back to the right). The uncertainty for the hydro-static pressure parameter was calculated to be 11.3 % and 10.9 % for the small (127 ± 34 µm) and larger particles (487 ± 98 µm). This deviation was consisted for the particle sizes investigated, which shows that the equipment was consistent through out every test conducted.

2.2. Bulk Modulus

The bulk modulus represents the ability of the material to withstand compaction. Shown in Figure 4 is the relationship between the bulk modulus (described in Equation (11)) as a function of the applied stress. This plotting convention is typically seen in literature [38, 39]. This figure accounts for load behavior carried out during compression. Notable in the figure is that the smaller particle size range reach a higher bulk modulus (760 MPa for 127 ± 34 μm) while the larger particles appear to reach a lower value (663 MPa for 309 ± 88 μm, and 648 MPa for 487 ± 98 μm). Similar studies conducted in the past showed that granular aluminum followed linear trends when loaded with a compressive stress of >300 MPa [40]. Interestingly, the aluminum particle trends observed were that larger particles (150 - 212 μm) had a slightly steeper slope than the smaller particles (53 - 75 μm) when looking at the B_{ep} as function of pressure. The bulk modulus is also more sensitive to the smaller particles (it increases at a faster rate). (309 ± 88 μm, 487 ± 98 μm). Propagation of error was likewise completed looking at the B_{ep}. Based on our calculations, the relative uncertainty was 11.7 % and 2.9 % for the small particle size (127 ± 34 μm) and large particle size (487 ± 98 μm) respectively.

2.3. Janssen Coefficient

Next, we investigate the Janssen coefficient which is used to relate the axial to the radial stresses which helps in simplifying analytical models when simulating triaxial compression behavior. Shown in Figure 5 is the relationship between the porosity and the Janssen coefficient for three particle size ranges. At higher porosity there is more variability in the Janssen coefficient across and within each particle size range. Specifically, larger particles have a higher Janssen coefficient for larger porosities. As the porosity is crushed out, (i.e reduced), the Janssen coefficient for all particle size ranges, converges to 0.23 (near 30 % porosity). The typical range for the Janssen constant seen in bulk materials has been noted to be 0.3-0.6 by [41]. These values are typically seen in round-like particle shapes and so the interesting behavior seen in Figure 5 is dependent on the elongated and rough edged particles. The relative uncertainty for the Janssen coefficient was 1.5 % and 1.7 % for the small (127 ± 34 μm) and larger (487 ± 98 μm) particles respectively.

2.4. Friction

Next, the wall friction effects can be probed by calculating the transmission ratio, which relates to the transmitted force through the material. Shown in Figure 6 is the transmission ratio as a function of applied load for all particle sizes. For a given applied stress the transmission ratio decreases for large particle sizes. For lower applied stresses, the values for lower applied stress is related to the compliance of the system. As the applied stress increases, the transmission ratio converges to 0.96. The small particles (127 ± 34 µm) approach convergence faster in comparison to larger particles (487 ± 98 µm). To account for the systematic error in the experiment, the uncertainty was calculated. For the small particles (127 ± 34 µm) the relative uncertainty was 6.5 % and for the large particles (487 ± 98 µm) the relative uncertainty was 6.6 %.

2.5. Failure analysis

Lastly, SEM images were taken of the consolidated SS316 to investigate failure features on the compacted specimens surfaces. Attempts were made to cut and polish the consolidated pucks after testing, but that only introduced further damage to the specimens. Shown in Figure 7a is the failure surface of the 309 ± 88 µm. This demonstrates that these particles withstood significant plastic deformation. Elongated laminate structures are noted (red arrows) on the surface, which are believed to be generated from particle shear stress during compaction. Shown in Figure 7b is the failure surface of the larger particles (487 ± 98 µm). There is noticeably more fracturing and cracking (red arrows). and the surface appeared to be more jagged in comparison to the smaller particles. Such evidence has been noted before by Roberts and Rowe [42]. Based on theoretical equations and experimental evidence, larger particles crack because the stress required for brittle fracture is less than the stress required for plastic flow. Likewise, smaller particles undergo plastic deformation due to the stress required is lower than the brittle deformation stress. These observations seen in our experiments are linked with the experimental data next in the Discussion.

3. Discussion

In this paper, we explored the mechanical response of granular SS316 for size ranges of: 127 ± 34 µm, 309 ± 88 µm, and 487 ± 98 µm. To accomplish this, we adapted a uniaxial compression experiment utilizing equipment and sensors: MTS 810, loader washer, displacement LVDT, and strain gauges. Similar experiments have been performed in the powder metallurgy and defense industries [43, 44, 45, 46, 47, 48], but limited data exists for stainless steel, however, it has been noted by Roberts and Rowe [42] that larger particles tend to fracture while smaller particles tend to plastically deform. Limitations to this work have been observed and noted. The use of (10) is limited based on the assumption of uniform radial stress and negligible friction. Kim et al. [33] underlined the limitations of our approach, using the TWC method. The other limitation of our design was the wall thickness of the crucible. The result of this would be decreased range in strain measurements. To resolve the issue additional calibration tests could be done. Furthermore, our design of the crucible was based on the assumption that the radial stress is uniform which would result in having the specimen friction-free, and therefore (10) is limited to the case where friction is negligible. However, we mitigated this issue by having the length of the strain gauge encompass the entire height of the specimen. Additional thought is given to the design parameters and so further calibration testing will be conducted to narrow the variability of the results and to validate the simplification of (7) from 3D to 2D space as highlighted by Meyer and Faber [46]. To better validate the material behavior, additional tests could be conducted to eliminate the outlying trends.

First we investigated the relationship between hydro-static pressure and porosity as a function of particle size. Other researchers have also looked at hydro-static pressure effects on granular material [44, 49]. In our experiments (Figure 3), it was observed that deviations in the hydro-static pressure among the particle sizes were sensitive for porosities greater than 30 %. For porosities less than 30 %, the behavior converges independent of particle size. This behavior has been observed before [50] when studying low carbon SS316 and the result was determined that densification of the material was sensitive to particle size. Cristofolini et al. [50] also demonstrated that initial porosity of the material highly influenced the loading path and that force dissipation during loading mostly originated from wall friction. These behaviors of granular stainless steel 316 have previously not been greatly considered or linked back to global granular response. We believe these linkages are valuable contributions in the additive manufacturing and other powder based industries. When calculating the uncertainty in porosity for the smallest and largest average particle sizes, we obtained values of 0.97 % for the 127 ± 34 µm size and 0.96 % for the 487 ± 98 µm.

Despite general insensitivities in particle size influence on the relationship between porosity and hydro-static pressure, it was observed that the bulk modulus was sensitive to particle size (Figure 4). In our experiment, we observed smaller particle sizes had higher bulk stiffness, were more sensitive to applied stress, and were more sensitive to unloading. Indeed, similar experiments [51, 52] demonstrated that particle size and compaction pressure influenced the mechanical response of the material. More importantly, the particle distribution with particles of different sizes required less energy to compact. In our experiments the ranging particle sizes dictated the mechanical response differences, which is observed to be associated with failure. Specifically, we note that smaller particles (127 ± 34 µm) undergo more plastic deformation (Figure 7a) as a consequence of compaction, while the larger particle (487 ± 98 µm) exhibits more fracture and micro-cracking (Figure 7b). Note that these particle size-dependent trends have been noted in other fields [53, 54, 55], and in particular this brittle-ductile transition behavior has been noted by Roberts and Rowe [42].

In addition to bulk response, we looked at the stress transmission ratio to investigate frictional behavior in compaction of granular SS316. In order to maximize the stress transmission through the material and minimize wall effects, the samples must maintain an aspect ratio of < 1. From our experiments, referring to Figure 6, the transmission ratio for the smaller particles (127 ± 34 µm), the curve begins a steep climb and later plateaus as the applied stress increases. Similar research conducted by Fleck and Cocks [30], showed that increasing the aspect ratio beyond 1 resulted in a significant decrease in the stress transmission. This leads us to better replicating an isotropic compaction environment. Other studies conducted by Perez-Gandarillas et al. [56] underlined the idea that lower axial transmission was observed with an increase in particle size. They concluded that part of the loading energy was consumed by the breakage of larger particles. Tracking these relationships allows for a better understanding of the complex behavior of fragmentation that could lead to more accurate failure modeling. Expanding on the idea of friction, additional research referencing frictional effects have been investigated by Staf et al. [57], where they determined the frictional coefficient, of granular ceramics, was a function of pressure. They determined that particle size and distribution were key factors in the compactability of a material. In contrary, the slope in the curve for the larger particles (487 ± 98 µm) in our experiments is shallower and does not increase as abruptly.

We further explored triaxial effects by studying the Janssen-Walker theory [58]. The Janssen coefficient is often used to simplify the relationship of granular stresses experienced in the axial and radial directions, so that the complex behavior can be simplified and implemented, for example, in existing material models to predict granular failure. Yousuff and Page [59] has shown this radial-axial relationship when studying iron powders. In our experiments, we were able to conclude for all three particle sizes tested the Janssen coefficient converged to a value of 0.23 (Figure 5). This explains that the radial wall stress was approximately 1/5 of the axial load regardless of the particle size. It was also observed that more variability exists for larger particle sizes (487 ± 98 µm) and porosities (50 %+). Altogether limited research exists on particle size dependencies and the observation highlights the importance of studying particle variability when researching granular metals. The idea of incorporating length scales into failure modeling, reduces the variability in predicting material behavior, but more importantly advances the forefront of powder material design.

4. Conclusion

A confined uniaxial compaction technique was used to determine the triaxial characteristics of granular SS316 as a function of ranging particle sizes. The results showed an influence of particle size in the compaction curves where porosity is related as a function of hydro-static pressure. In these experiments the bulk modulus was determined to be sensitive with respect to average particle sizes. This is believed to occur due to the failure mechanism that is likely related to the particle size, shape, and initial porosity. The smaller particles (127 ± 34 µm) appeared to exhibit higher flow stresses and underwent plastic deformation, while the larger particles (487 ± 98 µm) developed micro cracks which lead to fracture. Further research must be conducted to expand our understanding of particle size effects on mechanical properties of the material, to better establish failure regimes exhibited during triaxial loading conditions.

5. Acknowledgments

This research was sponsored by the Army Research Laboratory and was accomplished under Cooperative Agreement Number W911NF-12-2-0022. The views and conclusions contained in this document are those of the authors and should not be interpreted as representing the official policies, either expressed or implied, of the Army Research Laboratory or the U.S. Government. The U.S. Government is authorized to reproduce and distribute reprints for Government purposes notwithstanding any copyright notation herein. The author(s) would also like to express their support to Bernie Faulkner, Pouyan Motamedi, and Aidan Keaveny for their help in conducting the compression experiments, obtaining specimen images, and preliminary conceptualization respectively.

Bibliography

[1] Jeffrey Malcolm Benson and Ettienne Snyders. The need for powder characterisation in the additive manufacturing industry and the establishment of a national facility. *The South African Journal of Industrial Engineering*, 26(2):104, August 2015. ISSN 22247890. doi: 10.7166/26-2-951.

[2] M. H. Es-Saheb. Uniaxial strain rate effects in pharmaceutical powders during cold compaction. *Journal of Materials Science*, 27(15):4151–4159, 1992. ISSN 0022-2461, 1573-4803. doi: 10.1007/BF01105119.

[3] Andrew Feeney, Sakalima Sikaneta, Patrick Harkness, and Margaret Lucas. Ultrasonic compaction of granular geological materials. *Ultrasonics*, 76:136–144, April 2017. ISSN 0041624X. doi: 10.1016/j.ultras.2017.01.004.

[4] Jian-gu Qian, Jian-bo Gu, Xiao-qiang Gu, and Mao-song Huang. Discrete numerical modeling of granular materials considering crushability. *Journal of Mountain Science*, 14(4):758–770, April 2017. ISSN 1672-6316, 1993-0321. doi: 10.1007/s11629-016-4051-y.

[5] C. Dávalos, J. Cante, J.A. Hernández, and J. Oliver. On the numerical modeling of granular

material flows via the Particle Finite Element Method (PFEM). *International Journal of Solids and Structures*, 71:99–125, October 2015. ISSN 00207683. doi: 10.1016/j.ijsolstr.2015.06.013.

[6] M.J. Jiang, H.-S. Yu, and D. Harris. A novel discrete model for granular material incorporating rolling resistance. *Computers and Geotechnics*, 32(5):340–357, July 2005. ISSN 0266352X. doi: 10.1016/j.compgeo.2005.05.001.

[7] I M Cameron and D T Gethin. Exploration of die wall friction for powder compaction using a discrete finite element modelling technique. page 20, 2001. doi: 10.1088/0965-0393/9/4/304.

[8] D.T. Gethin, Roland Lewis, and Rajesh Ransing. A discrete deformable element approach for the compaction of powder systems. *Modelling and Simulation in Materials Science and Engineering*, 11:101, 12 2002. doi: 10.1088/0965-0393/11/1/308.

[9] Sachith Dunatunga and Ken Kamrin. Continuum modelling and simulation of granular flows through their many phases. *Journal of Fluid Mechanics*, 779:483–513, September 2015. ISSN 0022-1120, 1469-7645. doi: 10.1017/jfm.2015.383.

[10] J. D. Goddard. Continuum Modeling of Granular Media. *Applied Mechanics Reviews*, 66(5): 050801, May 2014. ISSN 0003-6900. doi: 10.1115/1.4026242.

[11] N.P. Kruyt, I. Agnolin, S. Luding, and L. Rothenburg. Micromechanical study of elastic moduli of loose granular materials. *Journal of the Mechanics and Physics of Solids*, 58(9):1286–1301, September 2010. ISSN 00225096. doi: 10.1016/j.jmps.2010.06.003.

[12] J. Tomas. Product Design of Cohesive Powders– Mechanical Properties, Compression and Flow Behavior. *Chemical Engineering & Technology*, 27(6):605–618, June 2004. ISSN 0930-7516, 1521-4125. doi: 10.1002/ceat.200406134.

[13] Conor P. Schlick, Austin B. Isner, Ben J. Freireich, Yi Fan, Paul B. Umbanhowar, Julio M. Ottino, and Richard M. Lueptow. A continuum approach for predicting segregation in flowing polydisperse granular materials. *Journal of Fluid Mechanics*, 797:95–109, June 2016. ISSN 0022-1120, 1469-7645. doi: 10.1017/jfm.2016.260.

[14] M.S. Kadiri, A. Michrafy, and J.A. Dodds. Pharmaceutical powders compaction: Experimental and numerical analysis of the density distribution. *Powder Technology*, 157(1-3):176–182, 2005. ISSN 00325910. doi: 10.1016/j.powtec.2005.05.025.

[15] A. Michrafy, M.S. Kadiri, and J.A. Dodds. Wall Friction and its Effects on the Density Distribution in the Compaction of Pharmaceutical Excipients. *Chemical Engineering Research and Design*, 81(8):946–952, September 2003. ISSN 02638762. doi: 10.1205/026387603322482185.

[16] David Train. An Investigatin into the Compaction of Powders. *Journal of Pharmacy and Pharmacology*, 8(1):745–761, 1956. ISSN 00223573. doi: 10.1111/j.2042-7158.1956.tb12206.x.

[17] Stefania Cacace, Ali Gökhan Demir, and Quirico Semeraro. Densification Mechanism for Different Types of Stainless Steel Powders in Selective Laser Melting. *Procedia CIRP*, 62: 475–480, 2017. ISSN 22128271. doi: 10.1016/j.procir.2016.06.010.

[18] John H. Martin, Brennan D. Yahata, Jacob M. Hundley, Justin A. Mayer, Tobias A. Schaedler, and Tresa M. Pollock. 3D printing of high-strength aluminium alloys. *Nature*, 549(7672):365–369, September 2017. ISSN 0028-0836, 1476-4687. doi: 10.1038/nature23894.

[19] Christopher T Schade, Thomas F Murphy, and Chris Walton. Development of atomized powders for additive manufacturing. page 11.

[20] A.B. Spierings, N. Herres, and G. Levy. Influence of the particle size distribution on surface quality and mechanical properties in AM steel parts. *Rapid Prototyping Journal*, 17(3):195–202, April 2011. ISSN 1355-2546. doi: 10.1108/13552541111124770.

[21] Yun Bai, Grady Wagner, and Christopher B. Williams. Effect of Particle Size Distribution on Powder Packing and Sintering in Binder Jetting Additive Manufacturing of Metals. *Journal of Manufacturing Science and Engineering*, 139(8):081019, June 2017. ISSN 1087-1357. doi: 10.1115/1.4036640.

[22] J.K. Prescott and R.A. Barnum. On powder flowability. *Pharmaceutical Technology*, 24:60–84+236, 01 2000.

[23] Naci Kurgan, Yavuz Sun, Bunyamin Cicek, and Hayrettin Ahlatci. Production of 316L stainless steel implant materials by powder metallurgy and investigation of their wear properties. *Chinese Science Bulletin*, 57(15):1873–1878, May 2012. ISSN 1001-6538, 1861-9541. doi: 10.1007/s11434-012-5022-5.

[24] N Bliss Shiny and S Gnanavel. Surface Modification of 316L Stainless Steel with Hydroxyapatite for Dental Implants. page 8, 2016.

[25] Bandar AL-Mangour. Powder metallurgy of stainless steel: State-of-the art, challenges, and development. page 45.

[26] Eric Maynard. Five fundamentals for effective blend sampling. *Powder and Bulk Engineering Magazine*, page 3, 2015.

[27] G. Bahar Basim and Mohsen Khalili. Particle size analysis on wide size distribution powders; effect of sampling and characterization technique. *Advanced Powder Technology*, 26(1):200–207, January 2015. ISSN 09218831. doi: 10.1016/j.apt.2014.09.009.

[28] Carl Levoguer. Using laser diffraction to measure particle size and distribution. *Metal Powder Report*, 68(3):15–18, May 2013. ISSN 00260657. doi: 10.1016/S0026-0657(13)70090-0.

[29] Roman Engeli, Thomas Etter, Simone Hovel, and Konrad Wegener. Processability of different IN738LC powder batches by selective laser melting. *Journal of Materials Processing Technology*, 229:484–491, March 2016. ISSN 09240136. doi: 10.1016/j.jmatprotec.2015.09.046.

[30] N. A Fleck and A. C. F Cocks. *IUTAM Symposium on Mechanics of Granular and Porous Materials: Proceedings of the IUTAM Symposium Held in Cambridge, U.K., 15-17 July 1996*. Springer Netherlands, Dordrecht, 1997. ISBN 978-94-011-5520-5. OCLC: 851391570.

[31] Mauricio Barrera and Hector Sanchez. Design of a Die for the Cold Compaction Calibration of Powdered Materials. *Suplemento de la Revista Latinoamericana de Metalurgia y Materiales S*, 1:223–234, 2009.

[32] Cesar A. Sciammarella and F. M. Sciammarella. *Experimental Mechanics of Solids*. Wiley, 2012.

[33] Daesung Kim, Sanghoon Kim, Hyunho Shin, and Kyong Yop Rhee. Feasibility of measuring the pressure vs. volume relationship of compressible solids using a thick-walled cylinder. *Powder Technology*, 322:490–496, December 2017. ISSN 00325910. doi: 10.1016/j.powtec.2017.08.052.

[34] G. Gustafsson, H.-Å. Häggblad, P. Jonsén, and P. Marklund. Determination of bulk properties and fracture data for iron ore pellets using instrumented confined compression experiments. *Powder Technology*, 241:19–27, June 2013. ISSN 00325910. doi: 10.1016/j.powtec.2013.02.030.

[35] Benjy Marks, Bjørnar Sandnes, Guillaume Dumazer, Jon Alm Eriksen, and Knut Jørgen Måløy. Compaction of granular material inside confined geometries. *Frontiers in Physics*, 3, June 2015. ISSN 2296-424X. doi: 10.3389/fphy.2015.00041.

[36] Herman J. C. Berendsen. *A Student's Guide to Data and Error Analysis*. Student's Guides. Cambridge University Press, 2011. doi: 10.1017/CBO9780511921247.

[37] R W Heckel. Density-Pressure Relationships in Powder Compaction. page 7.

[38] R. Holtzman, D. B. Silin, and T. W. Patzek. Mechanical properties of granular materials: A variational approach to grain-scale simulations. *International Journal for Numerical and Analytical Methods in Geomechanics*, 33(3):391–404, February 2009. ISSN 03639061, 10969853. doi: 10.1002/nag.725.

[39] V. Magnanimo, L. La Ragione, J. T. Jenkins, P. Wang, and H. A. Makse. Characterizing the shear and bulk moduli of an idealized granular material. *EPL (Europhysics Letters)*, 81(3): 34006, February 2008. ISSN 0295-5075, 1286-4854. doi: 10.1209/0295-5075/81/34006.

[40] N.W. Page and M.K. Warpenius. Loading relations for metal powders pressed to high density. *Powder Technology*, 61(1):87–94, April 1990. ISSN 00325910. doi: 10.1016/0032-5910(90)80069-B.

[41] Dietmar Schulze. Stresses in Silos. http://www.dietmar-schulze.de/spanne.html, 2019.

[42] R J Roberts and R C Rowe. Brittle-ductile transitions in die compaction of sodium chloride. page 5, 1989.

[43] Abhisek Choudhary, Pandu Ramavath, Papiya Biswas, Nukala Ravi, and Roy Johnson. Experimental Investigation on Flowability and Compaction Behavior of Spray Granulated Submicron Alumina Granules. *ISRN Ceramics*, 2013:1–6, 2013. ISSN 2090-7508. doi: 10.1155/2013/264194.

[44] J.Y. Huang, S.S. Hu, S.L. Xu, and S.N. Luo. Fractal crushing of granular materials under confined compression at different strain rates. *International Journal of Impact Engineering*, 106:259–265, August 2017. ISSN 0734743X. doi: 10.1016/j.ijimpeng.2017.04.021.

[45] Bin Liu, WenMao Huang, Lu Huang, and HaoWei Wang. Size-dependent compression deformation behaviors of high particle content B4C/Al composites. *Materials Science and Engineering: A*, 534:530–535, February 2012. ISSN 09215093. doi: 10.1016/j.msea.2011.12.003.

[46] L. W. Meyer and I. Faber. Investigations on granular ceramics and ceramic powder. *Le Journal de Physique IV*, 7(C3):C3–565, 1997.

[47] Biplob Mitra, Jon Hilden, and James D. Litster. Effects of the granule composition on the compaction behavior of deformable dry granules. *Powder Technology*, 291:487–498, April 2016. ISSN 00325910. doi: 10.1016/j.powtec.2016.01.009.

[48] Göran Frenning. Analysis of pharmaceutical powder compaction using multiplicative hyperelasto-plastic theory. *Powder Technology*, 172(2):103–112, March 2007. ISSN 00325910. doi: 10.1016/j.powtec.2006.11.001.

[49] Eduardo SuescunFlorez, Sina Kashuk, Magued Iskander, and Stephan Bless. Predicting the Uniaxial Compressive Response of Granular Media over a Wide Range of Strain Rates Using the Strain Energy Density Concept. *Journal of Dynamic Behavior of Materials*, 1(3):330–346, September 2015. ISSN 2199-7446, 2199-7454. doi: 10.1007/s40870-015-0028-0.

[50] I. Cristofolini, A. Molinari, G. Pederzini, and A. Rambelli. Study of the uniaxial cold compaction of AISI 316L stainless steel powders through single action tests. *Powder Technology*, 295:284–295, July 2016. ISSN 00325910. doi: 10.1016/j.powtec.2016.03.045.

[51] B V Ponraj and A Rajadurai. Parametric study on the compacting and sintering behaviour of powder metallurgical stainless steel components. (9):4, 2015.

[52] C. A. Lowe and A. W. Longbottom. Effect of particle distribution on the compaction behavior of granular beds. *Physics of Fluids*, 18(6):066101, 2006. ISSN 10706631. doi: 10.1063/1.2213641.

[53] A. Tarokh and A. Fakhimi. Relationship Between Grain Size and Fracture Properties of Rock. In *ARMA-2013-168*, page 10, ARMA, January 2013. American Rock Mechanics Association. ISBN 978-0-9894844-0-4.

[54] R. H. Brzesowsky, S. J. T. Hangx, N. Brantut, and C. J. Spiers. Compaction creep of sands due to time-dependent grain failure: Effects of chemical environment, applied stress, and grain size. *Journal of Geophysical Research: Solid Earth*, 119(10):7521–7541, October 2014. ISSN 21699313. doi: 10.1002/2014JB011277.

[55] Joanne T. Fredrich, Brian Evans, and Teng-Fong Wong. Effect of grain size on brittle and semibrittle strength: Implications for micromechanical modelling of failure in compression. *Journal of Geophysical Research*, 95(B7):10907, 1990. ISSN 0148-0227. doi: 10.1029/JB095iB07p10907.

[56] L. Perez-Gandarillas, A. Mazor, D. Souriou, O. Lecoq, and A. Michrafy. Compaction behaviour of dry granulated binary mixtures. *Powder Technology*, 285:62–67, November 2015. ISSN 00325910. doi: 10.1016/j.powtec.2015.05.003.

[57] Hjalmar Staf, Erik Olsson, Per Lindskog, and Per-Lennart Larsson. Determination of the Frictional Behavior at Compaction of Powder Materials Consisting of Spray-Dried Granules. *Journal of Materials Engineering and Performance*, 27(3):1308–1317, March 2018. ISSN 1059-9495, 1544-1024. doi: 10.1007/s11665-018-3205-1.

[58] R.M Nedderman. *Statics and Kinematics of Granular Materials - Method of Differential_slices.Pdf*. Cambridge University Press, October 2009. ISBN 978-0-511-60004-3.

[59] M. Yousuff and N.W. Page. Die stress and internal friction during quasi-static and dynamic powder compaction. *Powder Technology*, 76(3):299–307, 1993. ISSN 0032-5910. doi: https://doi.org/10.1016/S0032-5910(05)80011-7.

Table 1: Chemical composition of Alfa Aesar SS316 powder

Element	% Mass
C	0.022
Cr	16.860
Mo	2.200
Mn	0.100
P	0.019
S	0.011
Ni	11.190
Si	0.730
Fe	0.0001

Table 2: Particle size characterization observing the diameter distribution and circularity of each particle

Ø[µm]	D_{10}[µm]	D_{50}[µm]	D_{90}[µm]	Δ	C
127 ± 34	94	125	169	0.601	0.765 ± 0.116
309 ± 88	233	314	364	0.417	0.643 ± 0.127
487 ± 98	413	480	549	0.283	0.626 ± 0.146

Table 3: Compression Experiment Parameters and Results

Ø[µm]	m [mg]	V_o [mm^3]	ρ_o[kg m^{-3}]	ρ_f[kg m^{-3}]	ϕ_i [%]	ϕ_f [%]
127	0.43	137	3132	6230	60	22
309	0.33	122	2699	6281	66	21
487	0.31	118	2632	6142	67	23

Table 4: Propagation of error

Relative systematic error	Particle size 127 um	Particle size 487 um
Initial volume (V_o)	0.77%	0.90%
Porosity (ϕ)	0.97%	0.96%
Hydro-static pressure (σ_{hyd})	11%	10%
Bulk modulus (B_{ep})	12%	2.9%
Janssen coefficient (K)	1.5%	1.7%
Transmission ratio (T)	6.5%	6.6%

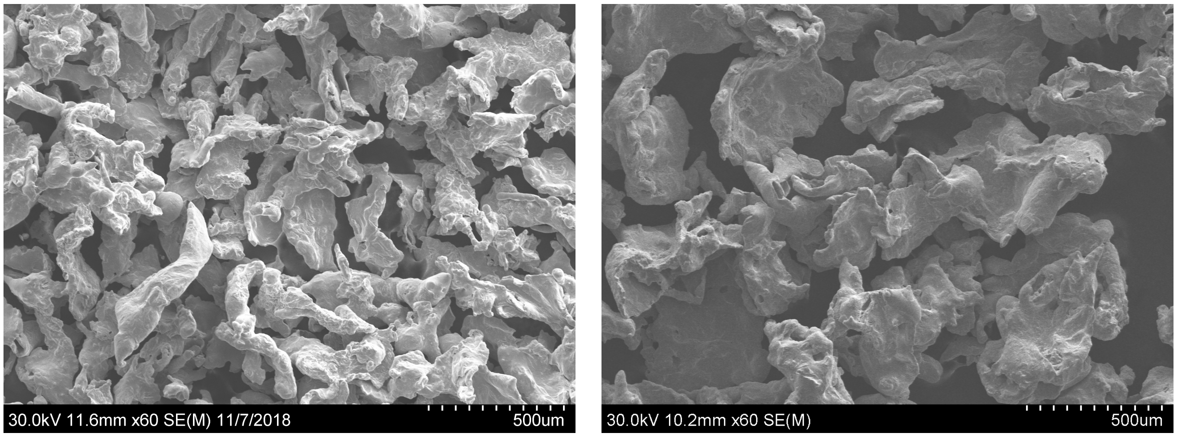

(a) (b)

Figure 1: SEM images of the SS316 powder at two different particle sizes: (a) 127 ± 34 µm and (b) 487 ± 98 µm respectively.

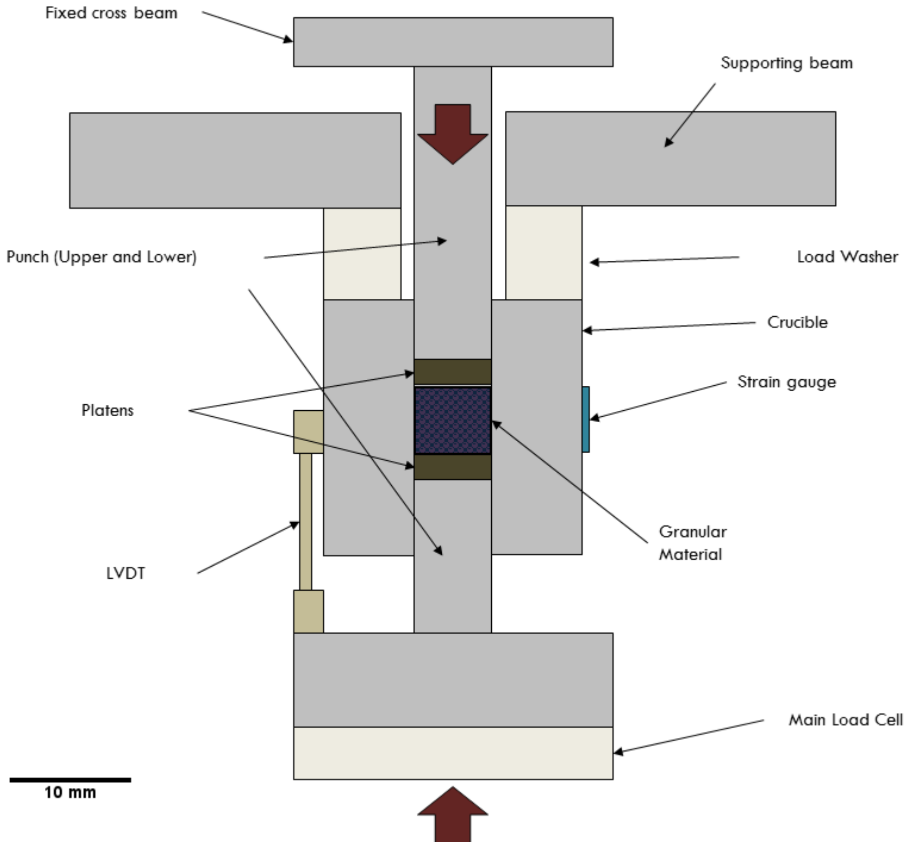

Figure 2: Schematic of the experimental set up illustrating key components and dimensions.

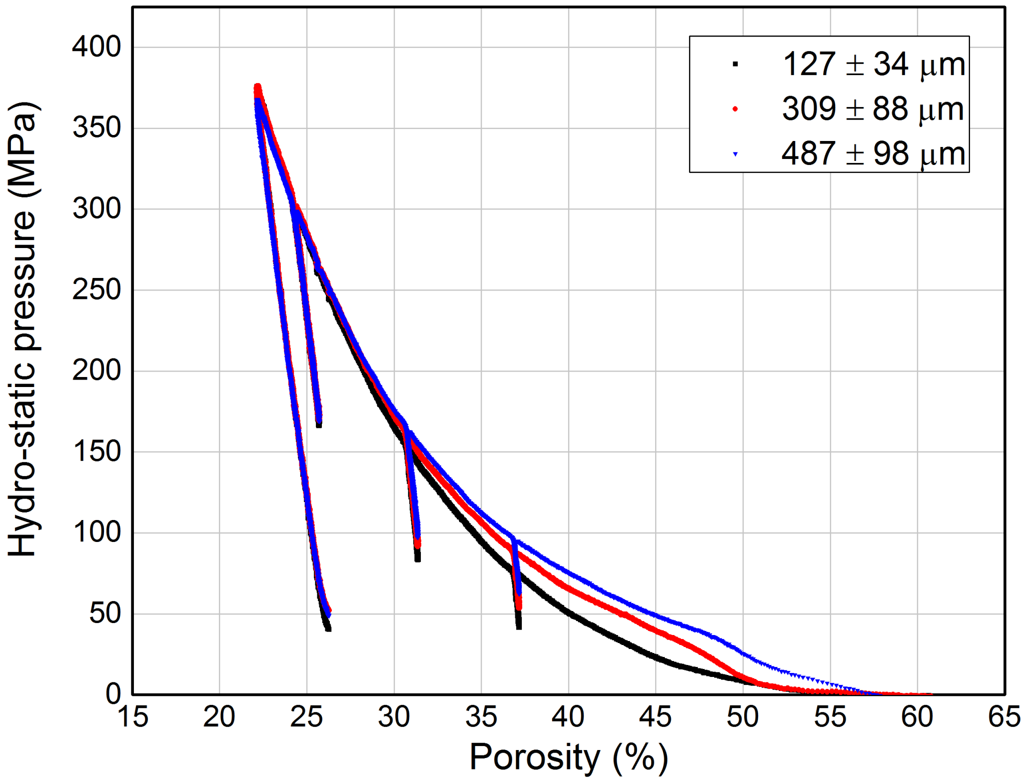

Figure 3: Quasi-static granular compaction response of SS316 powder for particle sizes of: 127 ± 34 μm, 309 ± 88 μm, 487 ± 98 μm.

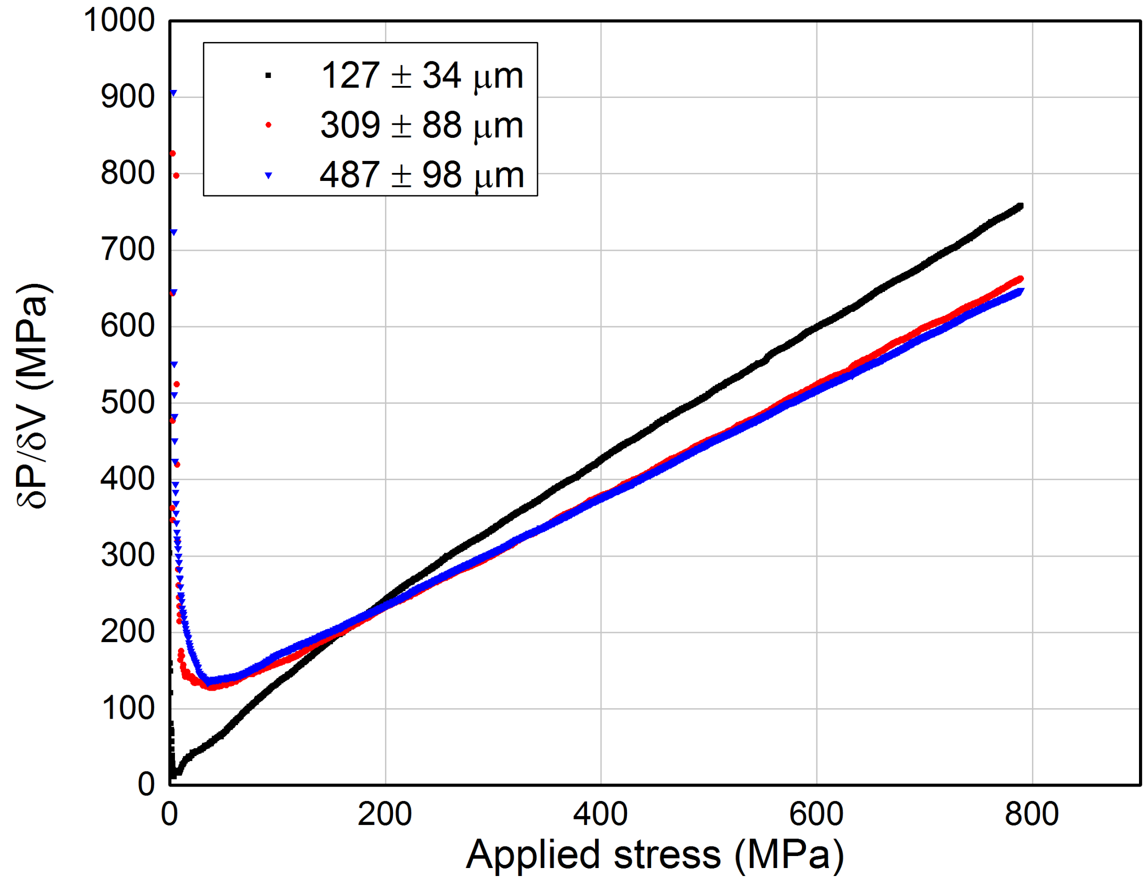

Figure 4: The bulk modulus as a function of applied stress for particle sizes of: 127 ± 34 µm, 309 ± 88 µm, 487 ± 98 µm.

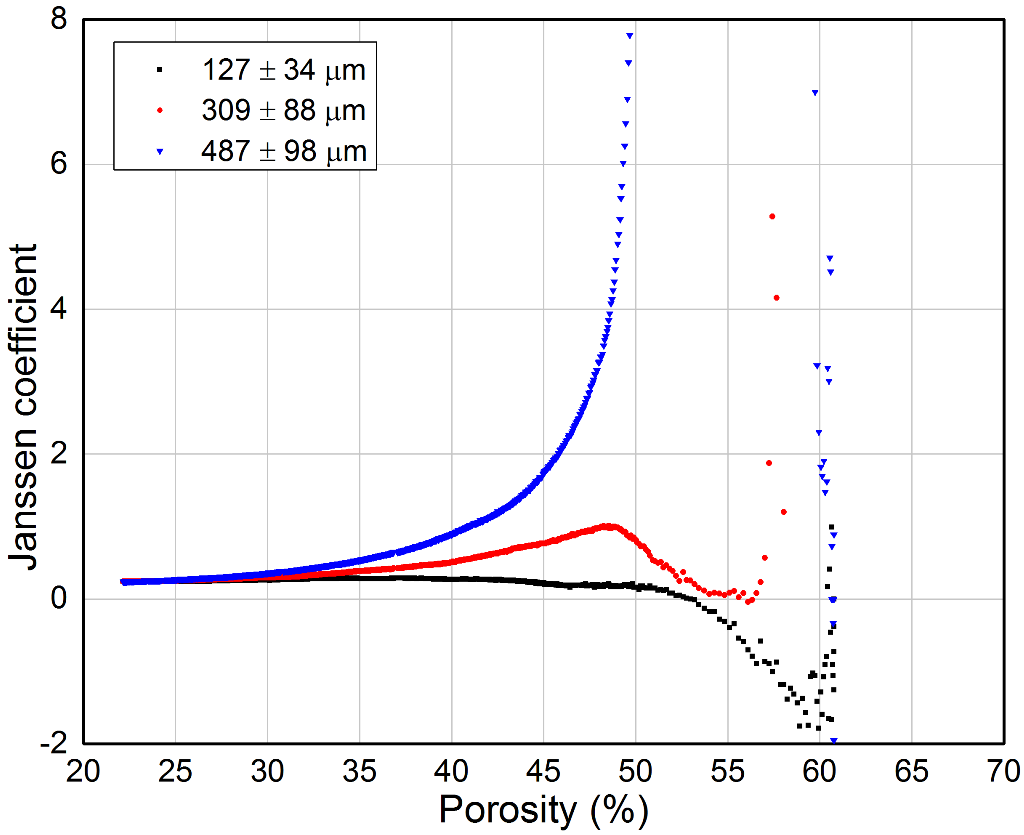

Figure 5: Janssen coefficient as a function of porosity for varying particle sizes: 127 ± 34 μm, 309 ± 88 μm, 487 ± 98 μm.

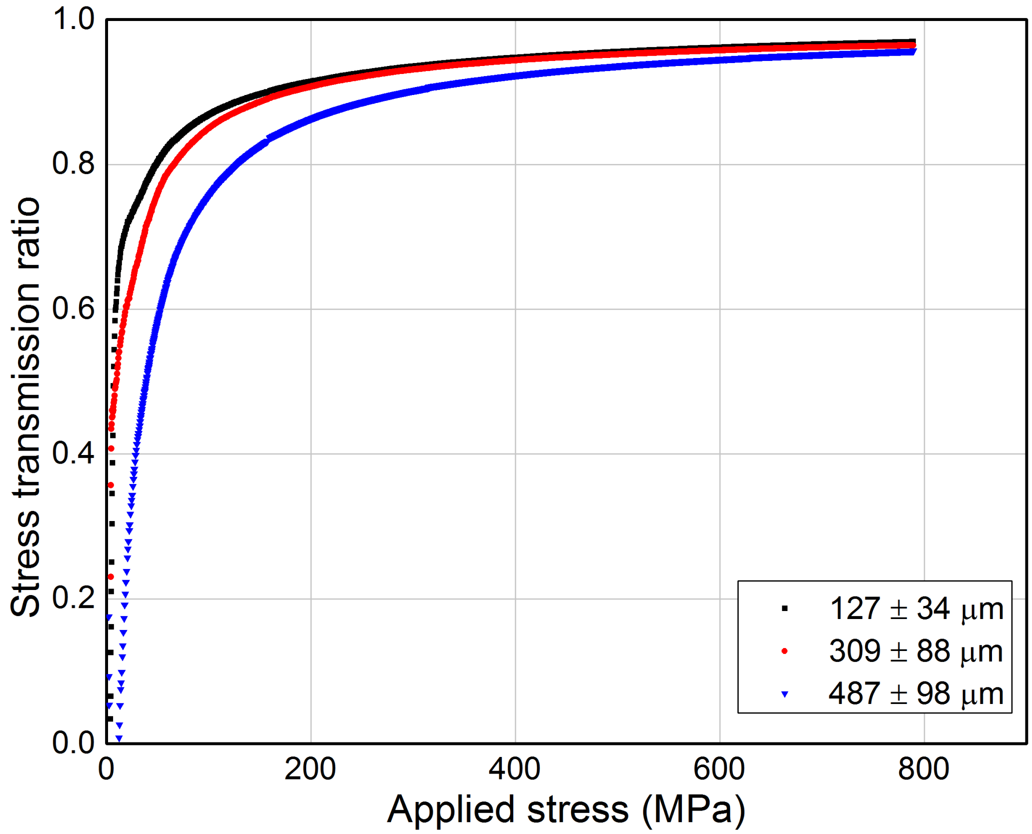

Figure 6: The transmission ratio relationship as a function of applied stress for different particle sizes: 127 ± 34 μm, 309 ± 88 μm, 487 ± 98 μm.

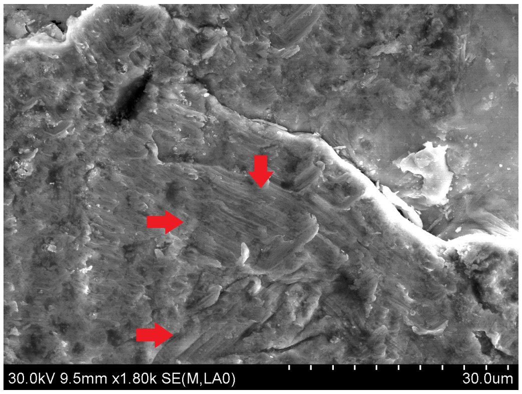

(a)

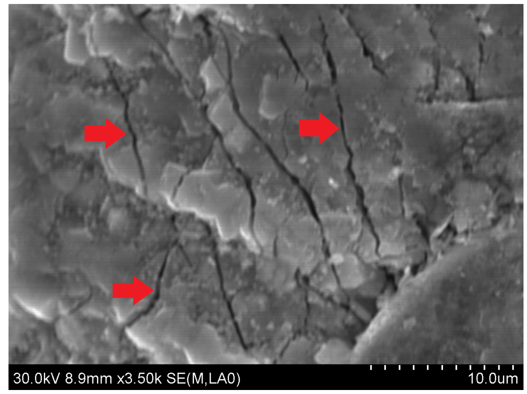

(b)

Figure 7: Post-experiment SEM images depicting failure mechanisms on the surface perpendicular to the applied load located at the top of the sample (in contact with the platen): (a) 309 ± 88 µm particle size and (b) 487 ± 98 µm particle size.

LaTeX Source Files
Click here to download LaTeX Source Files: Paper_SS315_Elsavier_Publication_Revision.zip

Data generated from experiments

Click here to download Supplementary Interactive Plot Data (CSV): Bulk Modulus submission.dat

Data generated from experiments

Click here to download Supplementary Interactive Plot Data (CSV): Hydro-static pressure submission.dat

Data generated from experiments

Click here to download Supplementary Interactive Plot Data (CSV): Janssen submission.dat

Data generated from experiments

Click here to download Supplementary Interactive Plot Data (CSV): Transmission ratio submission.dat